# Transport of intensity phase reconstruction to solve the twin image problem in holographic x-ray imaging

**M. Krenkel,* M. Bartels, and T. Salditt**

*Institut für Röntgenphysik, Universität Göttingen, Friedrich-Hund-Platz 1, 37077 Göttingen, Germany*

*mkrenke@gwdg.de

**Abstract:** We have implemented a deterministic method for solving the phase problem in hard x-ray in-line holography which overcomes the twin image problem. The phase distribution in the detector plane is retrieved by using two images with slightly different Fresnel numbers. We then use measured intensities and reconstructed phases in the detection plane to compute the exit wave in the sample plane. No further *a priori* information like a limited support or the assumption of pure phase objects is necessary so that it can be used for a wide range of complex samples. Using a nano-focused hard x-ray beam half period resolutions better than 30 nm are achieved.



**OCIS codes:** (340.7460) X-ray microscopy; (340.7440) X-ray imaging; (090.1995) Digital holography.

## References

1. K. A. Nugent, T. E. Gureyev, D. F. Cookson, D. Paganin, and Z. Barnea, "Quantitative phase imaging using hard x-rays," Phys. Rev. Lett. **77**, 2961–2964 (1996).
2. S. W. Wilkins, T. E. Gureyev, D. Gao, A. Pogany, and A. W. Stevenson, "Phase-contrast imaging using polychromatic hard X-rays," Nature **384**, 335–338 (1996).
3. K. A. Nugent, "Coherent methods in the x-ray sciences," Adv. Phys. **59**, 1–99 (2010).
4. T. Salditt, K. Giewekemeyer, C. Fuhse, S. P. Kruger, R. Tucoulou, and P. Cloetens, "Projection phase contrast microscopy with a hard x-ray nanofocused beam: Defocus and contrast transfer," Phys. Rev. B **79**, 184112(2009).
5. S. Mayo, P. Miller, S. Wilkins, T. Davis, D. Gao, T. Gureyev, D. Paganin, D. Parry, A. Pogany, and A. Stevenson, "Quantitative x-ray projection microscopy: phase-contrast and multi-spectral imaging." J. Microsc. **207**, 79–96 (2002).
6. P. Cloetens, W. Ludwig, J. Baruchel, D. V. Dyck, J. V. Landuyt, J. P. Guigay, and M. Schlenker, "Holotomography: Quantitative phase tomography with micrometer resolution using hard synchrotron radiation x rays," Appl. Phys. Lett. **75**, 2912–2914 (1999).
7. A. Burvall, U. Lundström, P. A. C. Takman, D. H. Larsson, and H. M. Hertz, "Phase retrieval in x-ray phase-contrast imaging suitable for tomography," Opt. Express **19**, 10359–10376 (2011).
8. B. D. Arhatari and A. G. Peele, "Optimisation of phase imaging geometry," Opt. Express **18**, 23727–23739 (2010).
9. J. Moosmann, R. Hofmann, A. Bronnikov, and T. Baumbach, "Nonlinear phase retrieval from single-distance radiograph," Opt. Express **18**, 25771–25785 (2010).
10. R. W. Gerchberg and W. O. Saxton, "A practical algorithm for the determination of phase from image and diffraction plane pictures," Optik (Jena) **35**, 237–246 (1972).
11. J. R. Fienup, "Phase retrieval algorithms: a comparison," Appl. Opt. **21**, 2758–2769 (1982).
12. K. Giewekemeyer, S. P. Krüger, S. Kalbfleisch, M. Bartels, C. Beta, and T. Salditt, "X-ray propagation microscopy of biological cells using waveguides as a quasipoint source," Phys. Rev. A **83**, 023804 (2011).

#179352 - $15.00 USD Received 21 Nov 2012; revised 16 Dec 2012; accepted 16 Dec 2012; published 23 Jan 2013

13. M. Bartels, M. Priebe, R. Wilke, S. Kruger, K. Giewekemeyer, S. Kalbfleisch, C. Olendrowitz, M. Sprung, and T. Salditt, "Low-dose three-dimensional hard x-ray imaging of bacterial cells," Opt. Nanoscopy **1**, 10 (2012).
14. T. E. Gureyev, T. J. Davis, A. Pogany, S. C. Mayo, and S. W. Wilkins, "Optical phase retrieval by use of first born- and rytov-type approximations," Appl. Opt. **43**, 2418–2430 (2004).
15. L. Turner, B. Dhal, J. Hayes, A. Mancuso, K. Nugent, D. Paterson, R. Scholten, C. Tran, and A. Peele, "X-ray phase imaging: Demonstration of extended conditions for homogeneous objects," Opt. Express **12**, 2960–2965 (2004).
16. D. P. J.B Tiller, A Barty and K. Nugent, "The holographic twin image problem: a deterministic phase solution," Opt. Comm. **183**, 7–14 (2000).
17. D. Gabor, "A new microscopic principle," Nature **161**, 777–778 (1948).
18. J. W. Goodman, *Introduction to Fourier optics* (Roberts & Company: Englewood, Colorado, 2005).
19. M. R. Teague, "Deterministic phase retrieval: a Green's function solution," J. Opt. Soc. Am. **73**, 1434–1441 (1983).
20. D. Paganin and K. A. Nugent, "Noninterferometric phase imaging with partially coherent light," Phys. Rev. Lett. **80**, 2586–2589 (1998).
21. D. M. Paganin, *Coherent X-ray Optics* (New York: Oxford University Press, 2006).
22. A. Groso, R. Abela, and M. Stampanoni, "Implementation of a fast method for high resolutionphase contrast tomography," Opt. Express **14**, 8103–8110 (2006).
23. B. L. Henke, E. M. Gullikson, and J. C. Davis, "X-ray interactions: photoabsorption, scattering, transmission, and reflection at E = 50-30,000 eV, Z = 1-92," Atomic Data and Nuclear Data Tables **54**, 181–342 (1993).
24. S. Kalbfleisch, H. Neubauer, S. P. Krüger, M. Bartels, M. Osterhoff, D. D. Mai, K. Giewekemeyer, B. Hartmann, M. Sprung, and T. Salditt, "The Göttingen holography endstation of beamline P10 at PETRA III/DESY," AIPConf.Proc. **1365**, 96–99 (2011).
25. T. Salditt, S. Kalbfleisch, M. Osterhoff, S. P. Krüger, M. Bartels, K. Giewekemeyer, H. Neubauer, and M. Sprung, "Partially coherent nano-focused x-ray radiation characterized by Talbot interferometry," Opt. Express **19**, 9656–9675 (2011).
26. S. P. Krüger, K. Giewekemeyer, S. Kalbfleisch, M. Bartels, H. Neubauer, and T. Salditt, "Sub-15 nm beam confinement by two crossed x-ray waveguides," Opt. Express **18**, 13492–13501 (2010).
27. C. Olendrowitz, M. Bartels, M. Krenkel, A. Beerlink, R. Mokso, M. Sprung, and T. Salditt, "Phase-contrast x-ray imaging and tomography of the nematode Caenorhabditis elegans," Phys. Med. Biol. **57**, 5309–5323 (2012).
28. M. Guizar-Sicairos, S. T. Thurman, and J. R. Fienup, "Efficient subpixel image registration algorithms," Opt. Lett. **33**, 156–158 (2008).
29. A. Pogany, D. Gao, and S. W. Wilkins, "Contrast and resolution in imaging with a microfocus x-ray source," Rev. Sci. Instrum. **68**, 2774–2782 (1997).
30. S. P. Krüger, H. Neubauer, M. Bartels, S. Kalbfleisch, K. Giewekemeyer, P. J. Wilbrandt, M. Sprung, and T. Salditt, "Sub-10 nm beam confinement by X-ray waveguides: design, fabrication and characterization of optical properties," J. Synchrotron Radiat. **19**, 227–236 (2012).
31. S. P. Krüger, "Optimization of waveguide optics for lensless x-ray imaging," Ph.D. thesis, Universität Göttingen (2010).
32. D. L. Misell, "An examination of an iterative method for the solution of the phase problem in optics and electron optics: Ii. sources of error," J. Phys. D: Appl. Phys **6**, 2217 (1973).
33. T. E. Gureyev, "Composite techniques for phase retrieval in the Fresnel region," Opt. Commun. **220**, 49 – 58 (2003).
34. D. Paganin, S. Mayo, T. Gureyev, P. Miller, and S. Wilkins, "Simultaneous phase and amplitude extraction from a single defocused image of a homogeneous object," J. Microsc. **206**, 33–40 (2002).
35. A. Liu, D. Paganin, L. Bourgeois, and P. Nakashima, "Projected thickness reconstruction from a single defocused transmission electron microscope image of an amorphous object," Ultramicroscopy **111**, 959–968 (2011).
36. T. Latychevskaia and H.-W. Fink, "Solution to the twin image problem in holography," Phys. Rev. Lett. **98**, 233901 (2007).
37. D. G. Voelz and M. C. Roggemann, "Digital simulation of scalar optical diffraction: revisiting chirp function sampling criteria and consequences," Appl. Opt. **48**, 6132–6142 (2009).
38. R. N. Wilke, M. Priebe, M. Bartels, K. Giewekemeyer, A. Diaz, P. Karvinen, and T. Salditt, "Hard x-ray imaging of bacterial cells: nano-diffraction and ptychographic reconstruction," Opt. Express **20**, 19232–19254 (2012).
39. M. Howells, T. Beetz, H. Chapman, C. Cui, J. Holton, C. Jacobsen, J. Kirz, E. Lima, S. Marchesini, H. Miao, D. Sayre, D. Shapiro, J. Spence, and D. Starodub, "An assessment of the resolution limitation due to radiation-damage in x-ray diffraction microscopy," J.Electron Spectrosc. **170**, 4–12 (2009).
40. K. Giewekemeyer, "A study on new approaches in coherent x-ray microscopy of biological specimens," Ph.D. thesis, Universität Göttingen (2011).

#179352 - $15.00 USD Received 21 Nov 2012; revised 16 Dec 2012; accepted 16 Dec 2012; published 23 Jan 2013

## 1. Introduction

X-ray propagation imaging is a full field imaging method based on contrast formation by free space propagation of a (coherent) wave behind the sample [1–3]. The technique enables the quantitative visualization of both the absorption coefficient and the phase shift in the sample, i.e. the real and imaginary component of the x-ray index of refraction $n(\mathbf{r}) = 1 - \delta(\mathbf{r}) + \mathrm{i}\beta(\mathbf{r})$. The two or three-dimensional index variation $n(\mathbf{r})$ in turn reflects the internal structure of the object both in terms of elemental composition and density. Compared to conventional absorption radiography and tomography, increased detection sensitivity and contrast for soft tissues and in general for low absorption samples is obtained. X-ray propagation imaging thus combines the advantageous penetration power for large specimens with increased contrast and sensitivity for small features, which may not exhibit sufficient absorption to be detected in conventional x-ray imaging. Importantly, by replacing plane wave illumination with curved wave fronts, propagation imaging can be combined with geometric magnification and applies for macroscopic as well as for nano-scale imaging. The fact that the technique needs no optical elements between object and detector presents a further advantage over other phase contrast methods (Zernike phase contrast, Talbot imaging) in terms of dose efficiency, which is important in particular for radiation in biological samples.

A central challenge of propagation imaging is the object reconstruction from a defocused image recorded by two-dimensional detectors at a (defocus) distance $z$ behind the object. To obtain the desired information on the sample from the recorded intensity pattern, the amplitude and phase of the wave directly behind the object needs to be reconstructed. In contrast to far-field diffraction patterns, the near-field intensity distributions (raw images) still show some resemblance with the object, but in general phase reconstruction is an essential requirement for quantitative imaging. Even if only qualitative gray values are needed to depict the shape or internal structure of the object, quantitative image reconstruction is preferable, since tomograms of raw projection images can in many cases not be segmented automatically, due to strong phase contrast fringes. The simplest form of reconstruction is the so-called holographic reconstruction by back propagation of the measured intensities. This leads to a sharper representation of the object, but is accompanied by spurious unfocused image components, notably by a twin image. Furthermore, owing to the oscillatory contrast transfer function (CTF) in near-field (Fresnel) diffraction [4, 5], some spatial frequencies cannot be retrieved. Quantitative reconstruction of the object's index of refraction is thus not possible by this approach.

Considerable efforts have therefore been undertaken in the past 15 years to devise proper reconstruction algorithms, which circumvent or solve the twin image problem associated with the holographic reconstruction, as reviewed in [3]. For example, improved reconstruction schemes based on one or several [6] defocus images or the knowledge of the CTF can be used. A review of reconstruction methods based on only a single image and the suitability for phase contrast tomography has been recently given in [7]. The so called Transport of Intensity Equation (TIE) is often applied for the reconstruction of near field images. This conventional use of the TIE is based on the assumption that the reconstructed phase distribution is a good approximation to the sample exit plane phase distribution [8]. However, these approaches often fail in the intermediate regime for larger defocus distances $z$ [9], when the contrast becomes stronger and more holographic features appear in the recorded intensity pattern. In this regime, it has been shown that iterative algorithms [10, 11], which are well established in (far-field) coherent diffractive imaging (CDI), can be applied after suitable generalization of the propagators and projection operators [12]. These algorithms solve the phase problem based on additional information about the wave function in the object plane. Well known examples are the constraint of a compact sample support or a pure phase contrast constraint based on negligible absorption. Iterative algorithms are probabilistic in nature, depending on (random) phase ini-

#179352 - $15.00 USD Received 21 Nov 2012; revised 16 Dec 2012; accepted 16 Dec 2012; published 23 Jan 2013

tialization, and may exhibit challenging convergence properties. In particular for tomography, single-step (deterministic) reconstruction techniques therefore present a valuable advantage, even though iterative algorithms with automated support determination and algorithmic control are also applicable to tomography [13].

In this work, we present a deterministic single-step approach, which we first study by simulations followed by subsequent synchrotron x-ray proof-of-concept experiments. The advantage of the approach is that it is applicable to a wide range of defocus distances, in particular also to the holographic regime, and that it is able to reconstruct the phase distribution of the sample exit plane without further *a priori* information and assumptions. Even though deterministic methods exist for the intermediate regime e.g. [14, 15], these methods are based on additional assumptions or linearisations. Furthermore, due to the zeros of the CTF, the reconstruction becomes difficult in the far holographic regime. The reconstruction schemes are based on the direct recovery of the phase distribution in the object plane from the measured intensities. Contrarily, here we use two neighboring image planes $z_1$ and $z_2 = z_1 + \Delta z$ to compute the phase not in the object plane but in the detection plane at $z_1$, followed by back propagation to the object plane. Furthermore no restrictive assumptions to the TIE were made. The additional phase information solves the twin image problem and the zeros in the CTF are automatically (partially) compensated by imposing the phase information. This method was used before for visible light [16] but has never been implemented for x-rays. Furthermore, the approximation can be easily controlled by adjusting $\Delta z$. No particular *a priori* knowledge on the wave in the sample plane is needed.

The paper is organized as follows: We first sketch out the fundamentals of the reconstruction approach in the context of scalar wave propagation in section 2. We then test the performance of the reconstruction algorithm by numerical simulations in section 3. The experimental details of the synchrotron experiment are given in section 4, followed by the presentation of the imaging results in section 5 and section 6, before section 7 closes the paper with a brief summary and conclusions.

## 2. Reconstruction algorithm

Before presenting and characterizing the reconstruction algorithm based on two imaging planes, i.e. images recorded at two defocus distances, we first repeat the essence of holographic reconstruction, which serves as a comparison. We then briefly sketch out the well established reconstruction approach based on the TIE equation, which provides the framework for the two plane solution presented here.

### *2.1. Holographic reconstruction*

For sufficiently large propagation distances $z$ or correspondingly small Fresnel numbers $F = a^2/(\lambda z)$ with $\lambda$ denoting the wavelength and $a$ a typical structure size, the recorded intensity distributions $I_z(x,y)$ are of holographic nature, i.e. significant interference effects of primary and scattered waves are observed. In contrast to the direct contrast regime at small $z$, the intensity of a given pixel is no longer a 'local' property of the corresponding sample point, but results from interference of waves scattered at many (neighboring) sample points as well as the primary wave which is assumed to be strong, since both absorption and scattering are weak in the hard x-ray regime for the samples considered here. Using this interference effect for phase sensitive ('holostic') imaging was the original idea of so-called in-line holography as invented by Gabor [17]. If the radiation is sufficiently coherent and monochromatic, one can reconstruct the original wave in the sample (exit) plane by back propagation of the recorded intensity pattern, i.e. the hologram. For numerical reconstruction (digital holography) a suitable propagation

#179352 - $15.00 USD Received 21 Nov 2012; revised 16 Dec 2012; accepted 16 Dec 2012; published 23 Jan 2013

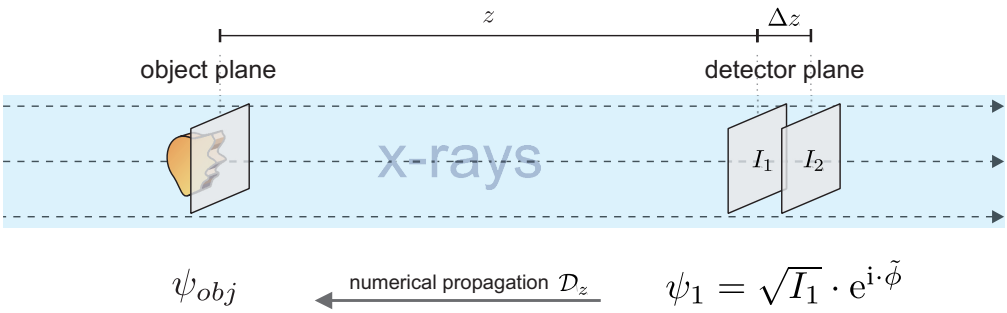


Fig. 1. General scheme of the Holo-TIE phase reconstruction: The wavefront $\psi_{obj}$ in the object plane, i.e. in the exit plane of the sample, is modified by the complex valued transmission function of the object. The intensity distribution of the field propagating along the optical axis, and measured in the two planes $z$ and $z+\Delta z$ with $\Delta z \ll z$, enables the reconstruction of an approximated phase $\tilde{\phi}$, for example in the first of the two planes located at a distance $z$ from the object plane. Along with the measured intensities in the 'detector plane' the reconstructed phase $\tilde{\phi}$ forms a completely specified wave $\psi_1$ which can be propagated back to the object plane in a straightforward manner.

method for paraxial waves $\psi$ is obtained from the angular spectrum method [18],

$$\psi(\mathbf{r}_\perp, z) = D_z\left(\psi(\mathbf{r}_\perp, 0)\right) = e^{\mathrm{i}kz}\mathscr{F}_\perp^{-1}\left[\exp\left(-\mathrm{i}\frac{z\left(k_x^2+k_y^2\right)}{2k}\right)\mathscr{F}_\perp\left(\psi(\mathbf{r}_\perp, 0)\right)\right], \qquad (1)$$

where $\psi(\mathbf{r}_\perp, z)$ is the wave function in a plane perpendicular to the optical axis at a distance $z$ along the optical axis, and $\psi(\mathbf{r}_\perp, 0)$ is the initial wave function. $\mathscr{F}_\perp$ denotes the Fourier transform in lateral coordinates, $k_x$ and $k_y$ are the lateral components of the wave vector $\mathbf{k}$ with modulus $k = 2\pi/\lambda$. As radiation detectors can only measure diffraction intensities $I_1(\mathbf{r}_\perp, z)$, the unknown wave function in the plane $z$ is usually approximated by the measured intensity distribution (hologram) without the phase information. This field is then propagated using Eq. (1), leading to the so-called holographic reconstruction:

$$\psi_{obj} = D_{-z}\left(I_1(\mathbf{r})\right) . \qquad (2)$$

The missing phase information produces artifacts in the reconstructed wave function, well known as the twin-image problem of in-line holography [18].

### *2.2. Phase retrieval for solving the twin image problem*

To solve the twin-image problem and to achieve a quantitative reconstruction, the phase distribution of the wave function needs to be reconstructed. The principle idea here is to reconstruct the phases first in the detection plane and then go to the object plane by back propagation which is an analytically exact operation. If phases $\phi_z(x,y)$ and intensities $I_z(x,y)$ are known in any plane, the wave function in every other plane and particularly in the object plane can be calculated by numerical propagation. The exact phases together with the measured intensities contain all information to solve the twin image problem and to correct for the zeros in the CTF. By reconstructing an approximate phase, the twin image and CTF artifacts are at least partially corrected, depending on how good the reconstructed phases approximate the exact phases.

Starting from the paraxial wave equation in vacuum

$$\left(\nabla_\perp^2 + 2\mathrm{i}k\partial_z\right)\psi(\mathbf{r}) = 0 , \qquad (3)$$

#179352 - $15.00 USD Received 21 Nov 2012; revised 16 Dec 2012; accepted 16 Dec 2012; published 23 Jan 2013

where $\nabla_\perp$ denotes the gradient in $x,y$ direction and $z$ the direction of the optical axis one can derive the TIE by writing the wave function $\psi(\mathbf{r}) = \sqrt{I(\mathbf{r})}e^{i\phi(\mathbf{r})}$ in terms of the measurable intensity distribution $I(\mathbf{r})$ and the unknown phase distribution $\phi(\mathbf{r})$, by inserting this Ansatz into (3) followed by some simplifications. The imaginary part of the resulting equation yields

$$\nabla_\perp \cdot (I(\mathbf{r})\nabla_\perp \phi(\mathbf{r})) = -k\frac{\partial I(\mathbf{r})}{\partial z} \,, \tag{4}$$

which is known as the TIE [19]. Following Paganin and Nugent [20], this equation can be solved to yield the phases by use of Fourier methods. To this end, it is assumed that a general potential $\xi$ exists, such that $I(\mathbf{r})\nabla_\perp \phi(\mathbf{r}) = \nabla_\perp \xi(\mathbf{r})$. With this assumption, some simple rewritings of Eq. (4) and the use of Pseudo-Differential-Operators for the inversion of the Laplacian, an expression for the phases can be derived

$$\phi(\mathbf{r}) = -k\nabla_\perp^{-2}\left(\nabla_\perp\left\{\frac{1}{I(\mathbf{r})}\nabla_\perp\left[\nabla_\perp^{-2}\left(\frac{\partial I(\mathbf{r})}{\partial z}\right)\right]\right\}\right) \,. \tag{5}$$

The Pseudo-Differential-Operators $\nabla_\perp^{-2}$ can be numerically implemented by a filtering operation in the Fourier space [21]

$$\nabla^{-2}(\cdot) = -\mathscr{F}^{-1}\left(\frac{1}{k_x^2+k_y^2+\alpha}\mathscr{F}(\cdot)\right) \,. \tag{6}$$

Basically this filter amplifies the low frequencies and suppresses high frequencies in the image. Here a regularization parameter $\alpha$ as in [22] is introduced to correct for experimental imperfections, like residual low frequency variations in the illumination wave front. Thus, if the derivative $\partial I(\mathbf{r})/\partial z$ of the intensity is known in some plane, the phases in this plane can be reconstructed. The required differential quotient can be approximated by the difference quotient of two measurable intensity distributions $I_1$ and $I_2$ (see Fig. 1), recorded in neighboring planes along the optical axis separated by $\Delta z$. Thus the reconstructed phases $\tilde{\phi}$ are only an approximation to the real phases $\phi$:

$$\tilde{\phi}(\mathbf{r}) = -\frac{k}{\Delta z}\nabla_\perp^{-2}\left(\nabla_\perp\left\{\frac{1}{I_1(\mathbf{r})}\nabla_\perp\left[\nabla_\perp^{-2}\left(I_1(\mathbf{r})-I_2(\mathbf{r})\right)\right]\right\}\right) \,. \tag{7}$$

Furthermore one has to choose one intensity for the division. One could measure a third image between both intensity distributions but as the reconstruction is based on approximations and regularizations this is ignored here and one of the measured images $I_1$, $I_2$ is chosen for the reconstruction. Here we take $I_1$ although in the experiments the unscaled image is chosen, which is typically the image with the smaller magnification to avoid upscaling. Due to this choice $\tilde{\phi}$ better approximates the phases in the plane of $I_1$. The reconstructed phase distribution $\tilde{\phi}$ together with the measured holographic amplitudes $\sqrt{I_1}$ can then be used as an approximation for the wave function at the detector plane, which becomes exact as $\Delta z \to 0$ and $\alpha \to 0$. Finally, this wave has to be back propagated to the object plane:

$$\psi_{obj} = D_{-z}\left(\psi_1 = \sqrt{I_1}\exp(\mathrm{i}\tilde{\phi})\right) \,. \tag{8}$$

For visible light this procedure was already implemented in [16], but an implementation and demonstration in the x-ray regime was so far missing. This general reconstruction scheme is illustrated in Fig. 1 and will be called Holo-TIE reconstruction in the following.

#179352 - $15.00 USD Received 21 Nov 2012; revised 16 Dec 2012; accepted 16 Dec 2012; published 23 Jan 2013

Table 1. Experimental details used for the Holo-TIE reconstruction and parameters used for the simulation. $E$ is the energy corresponding to the wavelength $\lambda$, $dx_{eff}$ denotes the (effective) pixel size, $z_{eff}$ the effective propagation distance and $\alpha$ is the regularization parameter. The Fresnel number $F$ is calculated for a typical structure size $a$ of 10 Pixels which allows a better comparison of the imaging regimes than taking the whole image or a fixed size due to the different numbers and sizes of pixel.

| | **Simulation** | **KB-setup** | **WG-setup (Fig. 6)** | **WG-setup (Fig. 7)** |
|---|---|---|---|---|
| $E$ [keV] | 12.398 | 13.8 | 13.6 | 13.6 |
| $\lambda$ [Å] | 1.000 | 0.898 | 0.911 | 0.911 |
| $dx_{eff}$ [nm] | 100 | 62.6 | 7.8 | 14.1 |
| $z_{eff}$ [mm] | 100 | 177.4 | 6.0 | 11.0 |
| $\Delta z_{eff}$ [mm] | 0.1 | 6.0 | 0.1 | 0.1 |
| $F$ | $100 \cdot 10^{-3}$ | $24.6 \cdot 10^{-3}$ | $11.1 \cdot 10^{-3}$ | $20.0 \cdot 10^{-3}$ |
| $\alpha$ | 0 | $5.0 \cdot 10^{-3}$ | $0.5 \cdot 10^{-3}$ | $1.0 \cdot 10^{-3}$ |
| exp. time [s] | - | 5 | 100 | 5 |

## 3. Simulations

To test the implemented algorithm, simulations of the experiment were performed. It was assumed that an object, consisting of a single material, is illuminated by a plane wave without magnification. The phase shifts range from $-0.45$ rad to 0 rad and the minimum transmission of the object was chosen to 94%, corresponding to the theoretical optical properties of 500 nm Ta at $E = 13.8\,\mathrm{keV}$ [23]. The image consists of $500 \times 500$ pixels, which were zero-padded to $1024 \times 1024$ pixels to reduce edge artifacts of the numerical propagation. Two holographic intensity distributions in the detector plane were calculated by an implementation of Eq. (1). The wavelength and geometric parameters for the simulation are shown in table 1. Noiseless data was assumed for the simulations.

Figure 2(a) and (b) show both simulated intensities $I_1$ and $I_2$. The difference of these images, shown in (c), is used for the Holo-TIE reconstruction to calculate the phase distribution in the detection plane, shown in (d). The classical holographic reconstruction (e), based on Eq. (2), results in an image which is overlayed by the twin image and has wrong absolute values. Using the reconstructed phases for the back propagation as in Eq. (8) provides a quantitative reconstruction shown in (f) without any artifacts arising from the twin image. The absence of experimental imperfections like noise or a non-uniform illumination allows a reconstruction without a regularization parameter $\alpha$. Furthermore a small distance $\Delta z$ can be used for an excellent approximation of the differential quotient. The choice of larger $\Delta z$ results in reconstruction artifacts, but also increases the signal (contrast) of the difference image, which is important for noisy data. The simulations (with added Poisson noise) can therefore be used to find the optimum experimental design for given sample and beam parameters.

## 4. Experimental realization with a magnifying x-ray setup

For the experimental realization, the Göttingen Instrument for NanoImaging with X-rays (GINIX) at the beamline P10 of the storage ring PETRA III, DESY in Hamburg, Germany was used [24, 25]. The photon energy was set to 13.8 keV and to 13.6 keV in two experimental parts denoted below by 'KB-setup' and 'WG-setup', respectively, using a $Si(111)$ double crystal monochromator with bandwidth $\Delta\lambda/\lambda \simeq 10^{-4}$. The beam was focused with fixed (elliptic) curvature Kirkpatrick-Baez (KB) mirrors to a focus size in the range of $150 - 400$ nm, depend-

#179352 - $15.00 USD Received 21 Nov 2012; revised 16 Dec 2012; accepted 16 Dec 2012; published 23 Jan 2013

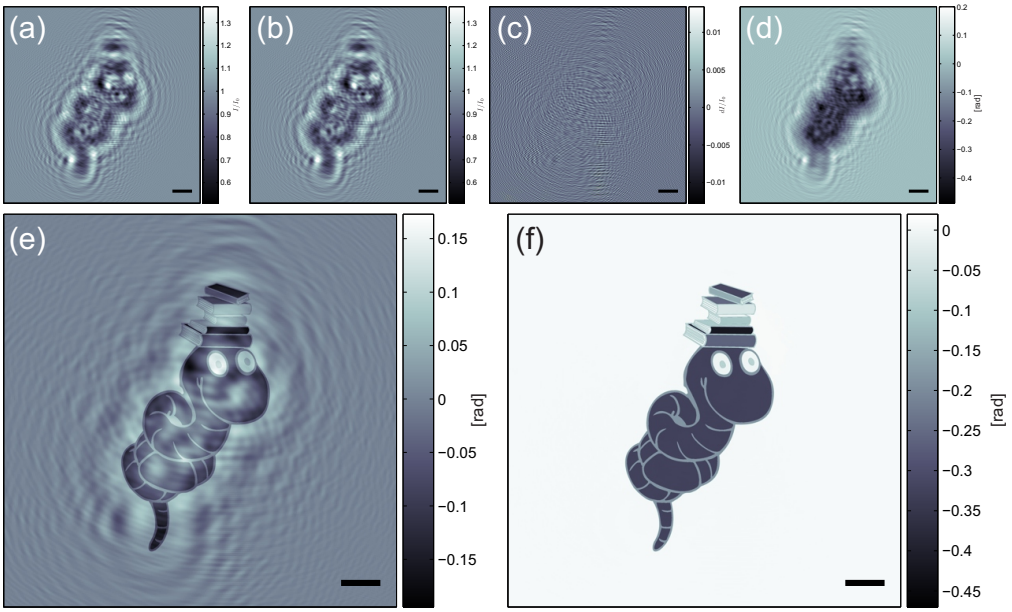


Fig. 2. Simulation results of the Holo-TIE reconstruction: (a), (b) Two intensity distributions of an object illuminated by a plane wave recorded in neighboring planes, in the holographic regime. (c) The difference of the images used to reconstruct the (d) phase in the detector plane. (e) The phase of the classical holographic reconstruction (Eq. (2)) shows contamination by the twin image. Together with the intensity shown in (a) and the reconstructed phase shown in (d), the correct wave function can be propagated back to the object plane (Eq. (8)). (f) The resulting phase in the object plane. Scale bars denote 5 µm.

ing on the exact beam setting. The focusing results in a divergent beam which can be used to image samples with geometric magnification. A resolution test pattern (ATN/XRESO-50HC, NTT-AT, Japan) which has a Siemens star pattern as the central object is used for the imaging experiments. The object consists of 500 nm Tantal in which the structure is written. The central region of the Siemens star shows structures down to 50 nm.

To suppress spurious high frequency beam variations, which are introduced by the imperfections on the mirror surface, a low pass filter is placed in the focal plane of the radiation. Two different objects for filtering were used in the following. The first (experiment is denoted by 'KB-setup') was a pinhole with 1.4 µm diameter which cuts only the tails of the KB beam in the focal plane. The pinhole was fabricated by focused ion beam polishing in a 20 µm Platinum foil.

For the second experiment (denoted by 'WG-setup'), a crossed multilayer x-ray waveguide (WG) [26] with 59 nm guiding layer was used, which reduces the effective source size to below 59 nm, at the expense of beam intensity. Figure 3(a) shows a sketch of the setup together with typical far field diffraction patterns of the (b) KB- and (c) waveguide experiment as measured by a pixel detector (Pilatus, Dectris). Note the higher divergence corresponding to the smaller effective source of the waveguide, which is also significantly smoother than the pinhole filtered KB-beam. This enables larger fields of view (FOV) for a given defocus distance $z$.

The image formation process in the divergent beam can be described by a simple variable transformation in an effective parallel beam geometry, which is computationally more convenient [21]. Figure 3(d) and (e) depicts this correspondence. The focus to object distance $z_{01}$ and

#179352 - $15.00 USD Received 21 Nov 2012; revised 16 Dec 2012; accepted 16 Dec 2012; published 23 Jan 2013

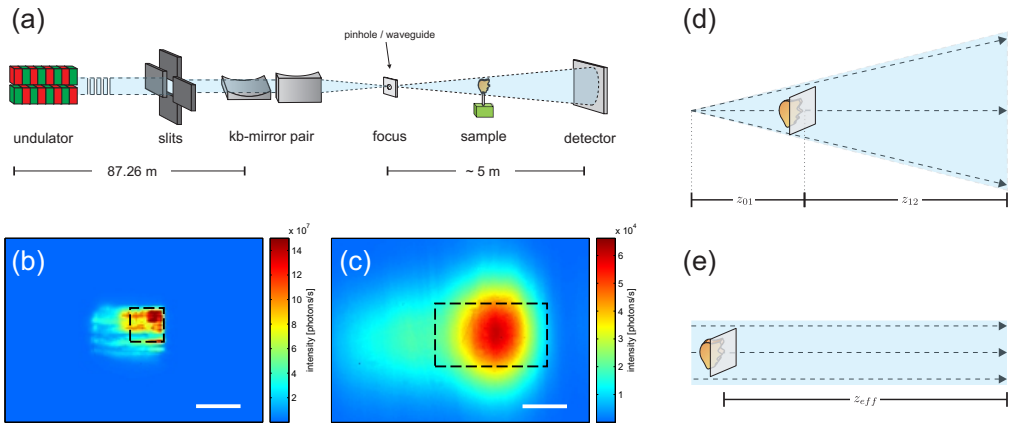


Fig. 3. Experimental setup used at the beamline P10 at PETRA III: (a) Sketch of the optical path. The beam is focused with a KB mirror system to some 100 nm. A pinhole or a waveguide is positioned in the focus to low pass filter the beam. The waveguide further confines the beam to less than 60 nm. (b) The resulting far field after using a pinhole with 1.4 µm diameter. (c) A far field created by the waveguide. The dashed rectangles denote the areas used in the KB- and WG-setup, respectively. Scale bars denote 5 mm on the detector. The divergent beam created by the focusing can be used to image samples with (d) a magnification setup which can be described in the (e) parallel beam geometry after a simple variable transformation.

the object to detector distance $z_{12}$ determine the geometrical magnification $M = (z_{01} + z_{12})/z_{01}$, and the effective propagation distance (in the effective parallel beam geometry) $z_{eff} = z_{12}/M$. In the experiment, the focus to detector distance was kept constant $z_{02} = z_{01} + z_{12} \simeq 5m$, with a 4 m long vacuum flight tube reducing absorption in air. By positioning the sample (in air) between focus and flight tube entrance, the magnifications and propagation distances needed, can be adjusted for the subsequent Holo-TIE reconstructions.

Two different x-ray detectors were used for the two different setups. For the 'KB-setup' experiment, a high resolution x-ray microscope (Optique Peter, France) was used, well fitted to the smaller KB beam cross section in the detection plane. The detector is based on a 20 µm LuAG:Ce scintillator foil (Crytur, Cz) of about 1 µm point spread function (PSF) which is observed by an optical microscope [27]. The microscope is equipped with a pco.2000 camera with $2048 \times 2048$ quadratic pixels of 7.4 µm edge length. Using a $\times 4$ objective this results in an effective pixel size of 1.85 µm. The low efficiency of this camera is compensated by the high flux of more than $10^{11}$ photons per second in the full KB-beam. The detector used in the waveguide experiment ('WG-setup') was a sCMOS camera (Photonic Science, GB) for visible light with a fiber optic connecting the chip with a custom scintillator (15 µm GdOS:Tb, Photonic Science) on the fiber optic. This camera has a pixel size of 6.54 µm with $1920 \times 1080$ pixels, hence a bigger active area, which is well suited for the larger WG beam cross section. The defocus images with the object were recorded, and normalized to measurements of the empty beam (empty beam division). These corrected images are denoted normalized holograms in the following, and constitute the input for the subsequent reconstruction.

Figure 4 shows the recording scheme for the experiments. Figures 4(b) and 4(d) show empty beam images, recorded without a sample in the beam, for the 'KB-setup' and the 'WG-setup', respectively. Holograms of a test pattern (ATN/XRESO-50HC, NTT-AT, Japan) can be recorded at the desired defocus distance, as shown in Fig. 4(c) and (e). The non-uniformity of the beam

#179352 - $15.00 USD Received 21 Nov 2012; revised 16 Dec 2012; accepted 16 Dec 2012; published 23 Jan 2013

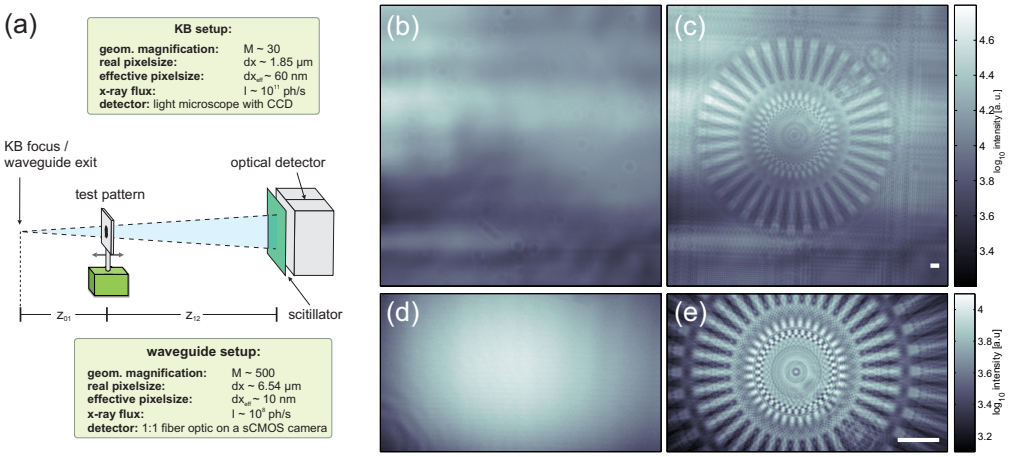


Fig. 4. (a) The general recording scheme. (b) A typical empty beam image recorded in the 'KB-setup' experiment. Due to the high flux of the KB-beam, it is possible to use a high resolution detector. Compared to other available detectors, this detector based on optical microscopy of a scintillation foil requires smaller geometric magnification for desired object pixel size, and hence enables larger defocus distances $z$. This combination is well suited for the KB beam with relatively small divergence. (c) The corresponding raw image of a test structure. In the waveguide setup ('WG-setup'), a more efficient detector can be used (fiber coupled sCMOS camera) with larger pixels and larger active area, well matched to the larger divergence. (d) A typical empty beam image, with comparatively less artifacts from high frequency wave front distortions, which compromise image quality. (e) A corresponding raw image of the test structure. The scale bars denote 4 µm.

can be partially compensated by empty beam correction. The test structure is moved along the optical axis to record images with different effective propagation distances and magnifications, hence with different Fresnel numbers $F$. Two images spaced by $\Delta z$ can then be used for the Holo-TIE reconstruction.

## 5. Experimental results

### *5.1. KB-setup*

Figures 5(a) and (b) show two recorded normalized holograms in the KB beam with a defocus variation of $\Delta z = 6.4\,\mathrm{mm}$. The acquisition time was 5 seconds for each raw image and empty beam image. The focus to detector distance was $z_{02} = 5.42\,\mathrm{m}$, the object was placed $z_{01} = 0.19\,\mathrm{m}$ behind the focus and moved towards the focus for the second image. All relevant parameters for the reconstruction are listed in table 1. Due to the divergence of the beam, the magnification of the both images is slightly different ($M_1/M_2 = 0.965$). To enable the subtraction of the images the image with smaller effective pixel size is downscaled to the larger pixel size using a bicubic interpolation algorithm (Matlab). After resizing one of the images, the two images were aligned using a registration algorithm described in [28]. The shifting of the images results in $1969 \times 1945$ remaining pixels.

Figure 5(c) shows the resulting difference image which can be used to approximate the differential $\partial_z I$ in Eq. (5). Note that this difference image shows low frequency artifacts, which result from variations of the illumination wave front. These variations can be compensated by the use of a regularization parameter. If the regularization parameter $\alpha$ is chosen too large,

#179352 - $15.00 USD Received 21 Nov 2012; revised 16 Dec 2012; accepted 16 Dec 2012; published 23 Jan 2013

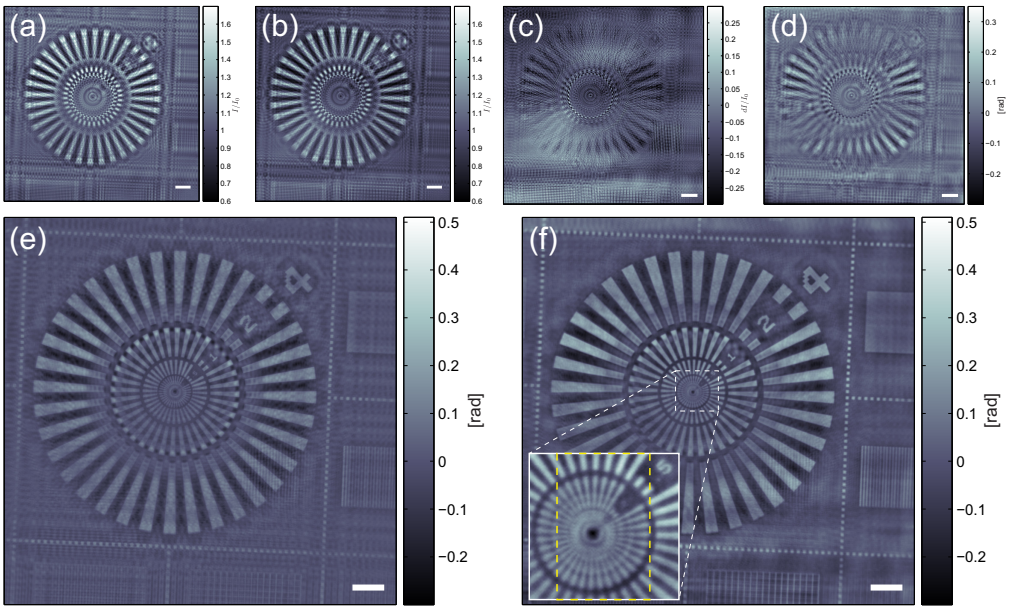


Fig. 5. Experimental results of the Holo-TIE reconstruction in the KB experiment: (a), (b) Two empty beam corrected intensity distributions recorded with small defocus difference $\Delta z$. (c) Difference image, computed from (a) and (b) after compensating for lateral shift and different magnifications. (d) Phase reconstruction in the detector plane, computed from (a) and (b), using a regularization parameter compensating for non-uniformity in the illumination. (e) Conventional holographic reconstruction (Eq. (2)), showing artifacts due to the twin image. (f) The regularized Holo-TIE reconstruction (Eq. (8)). The zeros in the contrast-transfer-function are partially compensated in the Holo-TIE reconstruction. The inset shows a zoom of the central region (contrast adjusted). The 200 nm lines and spaces of the test structure are resolved. The dashed line in the inset shows approximately the region imaged in the WG-setup (Fig. 6). Scale bars denote 10 µm.

it eliminates the filter used for the inversion of the Laplacian, whereas if chosen too small, it amplifies spurious beam variations too strongly. Hence, in the limit of large $\alpha$ the Holo-TIE reconstruction (Eq. (8)) yields the same reconstruction as the holographic reconstruction (Eq. (2)). Subfigure (d) shows the reconstructed phase distribution in the detector plane for a regularization parameter $\alpha = 5 \cdot 10^{-3}$. The resulting phase distribution in the object plane of the Holo-TIE reconstruction is shown in Fig. 5(f). The central region, which exhibits the smallest structures of the test object, is shown in the inset. The smallest resolvable structure has a size of 200 nm, which can be expected based on the KB source size. The field of view has a size of about $120 \times 120\,\mu\text{m}^2$. As can be seen, the Holo-TIE reconstruction calculated via Eq. (8) is less affected by the twin image compared to the classical holographic reconstruction (Eq. (2)) shown in Fig. 5(e). Image frequencies which are missing owing to the zeros in the CTF [4, 29] are partially compensated for by the phase reconstruction.

### *5.2. Experimental results of the waveguide-setup*

In order to improve the resolution, a smaller effective source is needed. Placing a x-ray waveguide in the focal plane of the KB, the effective source size is significantly reduced. Here we have used a waveguide with 59 nm guiding layer thickness resulting in minimum beam size of 16 nm (Full Width Half Maximum), according to finite difference simulations. Two

#179352 - $15.00 USD Received 21 Nov 2012; revised 16 Dec 2012; accepted 16 Dec 2012; published 23 Jan 2013

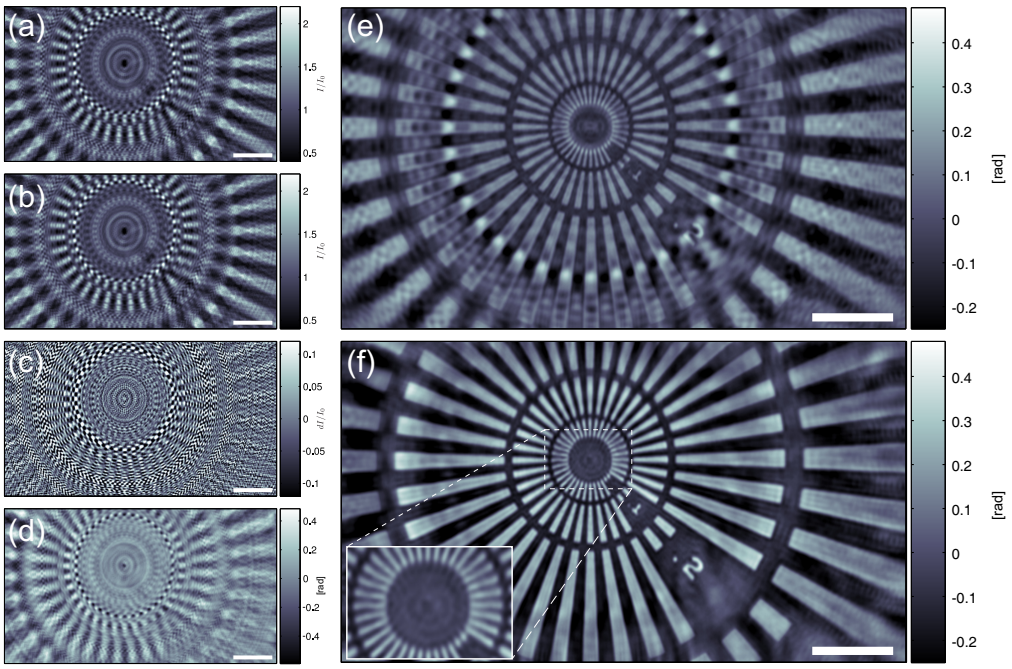


Fig. 6. Experimental results of the Holo-TIE reconstruction in the waveguide experiment ('WG-setup' setting), presented in the same sequence as in Fig. 5: (a), (b) The two empty beam corrected images, and (c) the corresponding difference image after resizing and alignment. (d) The reconstructed phase distribution in the detector plane, and (f) the Holo-TIE reconstruction (Eq. (8)), which is found to exhibit less artifacts than (e) the holographic reconstruction (Eq. (2)). Compared to the reconstruction in Fig. 5 the Holo-TIE shows much less artifacts which is a result of the smaller regularization parameter. The central region in (f) is magnified in the inset. The inner structure size is 50 nm lines and spaces, which are clearly resolved in all directions. All scale bars denote 2 μm.

planar waveguides are combined in a crossed geometry to provide beam confinement in both directions [30, 31]. The flux exiting the waveguide was $2.59 \cdot 10^8$ photons per second. The smaller effective focal size results in a larger beam divergence, and hence a larger field of view (FOV) at given $z_{01}$. Correspondingly, at constant FOV (e.g. selected according to sample size), the magnification $M$ achievable with a given detector position is higher. In the present case, effective pixel sizes in the sample plane of about 8 nm were obtained by placing the test structure at a distance $z_{01} = 6.1$ mm, while the focus to detector distance was $z_{02} = 5.09\,\mathrm{m}$. Figures 6(a) and (b) show two normalized holograms recorded in this setting. The exposure time in this data set was $10 \times 10$ seconds per raw and empty beam image. The empty beam images were recorded between two raw images by moving the test structure in and out of the beam. To correct for the imperfect movements of the motors, the images were aligned to each other with an algorithm described in [28]. The average of all aligned images was taken for the Holo-TIE reconstruction.

The procedure for the Holo-TIE reconstruction is the same as in the KB experiment described above. The magnification difference ($M_1/M_2 = 0.984$) is compensated by resizing the images, followed by subsequently registration. Figure 6(c) shows the resulting difference image. Compared to the 'KB-setup' setting, this difference is not so much affected by beam variations. The

#179352 - $15.00 USD Received 21 Nov 2012; revised 16 Dec 2012; accepted 16 Dec 2012; published 23 Jan 2013

waveguide does not only filter the radiation but also provides a more stable effective source. A further reason for the higher image quality can be attributed to the smoothness of the beam which exhibits a profile which is closer to a Gaussian than in the KB-setup. Therefore, a significantly smaller regularization parameter of $\alpha = 5 \cdot 10^{-4}$ was chosen. The resulting phase reconstruction in the detector plane is shown in Fig. 6(d). The classical holographic reconstruction retrieved by Eq. (2) is shown in (e) and the resulting Holo-TIE reconstruction (Eq. (8)) is shown in (f). In the back propagation step, the astigmatism of the waveguide is considered by introducing an anisotropic Fresnel propagator.

While significant distortions due to the twin image and zeros of the contrast transfer function are observed in the holographic reconstruction, the Holo-TIE reconstruction minimizes these artifacts, and exhibits a rather uniform representation of the patterned areas. The smallest structures in the central region of the test object of 50 nm width can be clearly resolved as the magnifying inset shows.

## 6. Hybrid approach

The exposure times for the images in Fig. 6 were quite long (100 s) to reduce noise effects in the reconstructions. Figure 7(a) shows the Holo-TIE reconstruction of another data set with a shorter exposure time of 5 s. Furthermore the FOV was increased by increasing the focus to object distance (see table 1). The reconstruction shows some cloudy background structure (noise) which is introduced in the filtering step to reconstruct the detector plane phase distribution. We attribute this cloudy noise to shot noise in the difference image. In the following we present a hybrid approach by using a modified Gerchberg-Saxton (GS) type algorithm [10, 32] to reduce the noise in the short exposure reconstructions.

The idea is to initialize the iterative algorithms by the Holo-TIE reconstruction, followed by a rather small number of iterations carried out to remove or reduce the noise artifacts. Note that near field TIE reconstruction with inferior image quality was proposed as an initial guess for iterative algorithms [33]. Here we demonstrate the hybrid approach by passing the Holo-TIE solution over to an iterative modified GS algorithm. The GS algorithm used here works as follow: An initial guess in the specimen plane is numerically propagated to the detector plane by using Eq. (1). In the detector plane the wave function is projected to the measured amplitudes and propagated back to the object plane where additional constraint can be used to update the wave function. Instead of using a second measured intensity distribution in the object plane we make use of the fact that the object consists of a single material. This provides additional constraints to the wave function, which can result in reduced noise as shown in near field applications [34,35]. We have recently used a constraint for iterative reconstructions based on this assumption [27] which is described here in detail: The assumption of a single material motivates the use of a fixed coupling between absorption and phase shift $\beta(x,y,z) = \gamma\delta(x,y,z)$ for the real and imaginary part of the refractive index $n = 1 - \delta + \mathrm{i}\beta$. The wave field behind the sample is then written as

$$\psi(x,y) \propto \exp\left(-k\beta\,\tau(x,y)\right) \times \exp\left(-\mathrm{i}k\delta\,\tau(x,y)\right) \ , \tag{9}$$

with the density $\tau(x,y)$ projected along the optical axis $z$. The constraint which is used to update the wave function in the object plane is thus formulated

$$\mathrm{abs}(\psi) = \mathrm{e}^{\gamma \cdot \mathrm{angle}(\psi)} \ . \tag{10}$$

For tantalum at the given photon energy, the coupling parameter value is $\gamma = 0.1342$ [23]. In addition, the amplitudes are forced to be smaller than one, see also [36]. For the reconstruction,

#179352 - $15.00 USD Received 21 Nov 2012; revised 16 Dec 2012; accepted 16 Dec 2012; published 23 Jan 2013

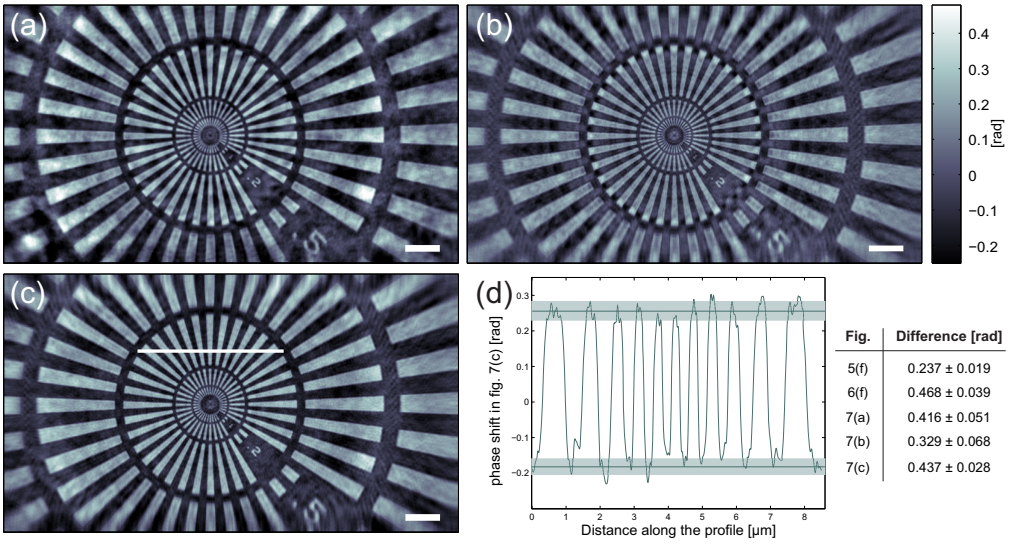


Fig. 7. Experimental results of the hybrid approach. (a) The Holo-TIE reconstruction (Eq. (8)) of the short exposure data set with larger FOV. The cloudy background is attributed to shot noise in the difference image. (b) The phase distribution obtained by running a modified GS algorithm for 5 iterations after priming the algorithm with the holographic reconstruction, and (c) the same for the Holo-TIE initial guess, showing a much more uniform structure. The cloudy noise of the Holo-TIE reconstruction is significantly reduced by application of only 5 iterations. (d) A profile along the line shown in (c). Fitting an error function to a step in the central region yields a FWHM of 59 nm. Line profiles as shown here were used to estimate the phase difference between bright and dark regions of the structure shown in the table. The scale bars denote 2 µm.

only 5 iterations were carried out, which took about 105 seconds with a Matlab implementation on a modern personal computer (3 GHz Intel processor) with proper sampling of the propagation (see e.g. [37]). Figure 7 shows the resulting phase distribution with (b) the holographic reconstruction as initial guess and (c) the Holo-TIE result as initial guess. While (b) still shows some twin image artifacts, the Holo-TIE initialization exhibits superior image quality, and thus constitutes an optimized and efficient hybrid approach. The cloudy background noise present in the pure Holo-TIE reconstruction shown in Fig. 7(a) is strongly reduced by the few iterations.

## 7. Discussion and conclusion

From the reconstructions presented in the preceding sections we can conclude that the Holo-TIE approach offers a robust one-step reconstruction, without the need for restrictive sample constraints, and applicable to a wide range of defocus distances, including the holographic regime relevant for projection geometry. As a fast one-step reconstruction procedure, Holo-TIE is ideal for phasing tomographic data with many images. Finally, let us briefly discuss the quantitativeness of the reconstructions and the dose efficiency of the imaging approach presented here.

To estimate the quantitativeness of the reconstruction, line profiles through the phase distribution were analyzed. A suitable region was chosen by visual inspection for each reconstruction and line profiles were evaluated along several grooves of the test structure. An example of such a line scan is shown in Fig. 7(d). The values above and below a certain threshold are used to obtain an averaged phase shift of the bright and dark areas of the test pattern. The solid line in

#179352 - $15.00 USD Received 21 Nov 2012; revised 16 Dec 2012; accepted 16 Dec 2012; published 23 Jan 2013

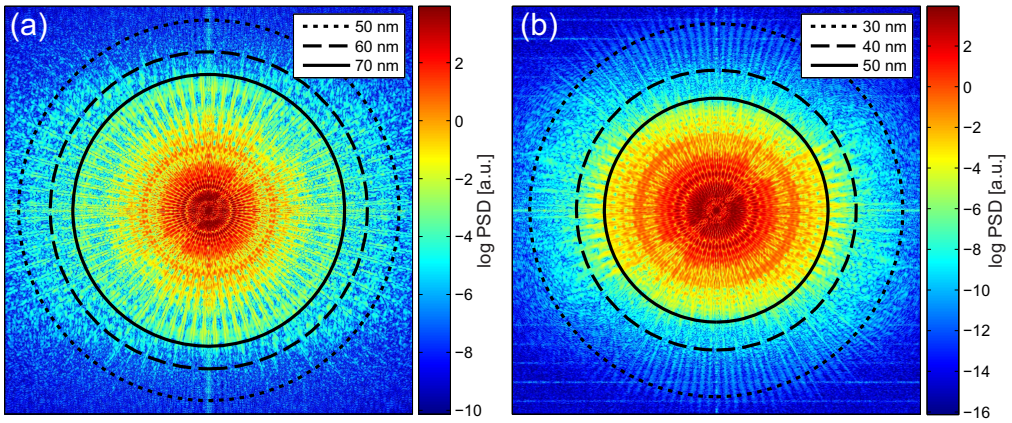


Fig. 8. (a) Power spectral densities of the hybrid approach with the short exposure ($2 \times 5$ seconds) data set (Fig. 7(c)) and (b) of the Holo-TIE reconstruction of the long exposure ($2 \times 100$ seconds) data set with smaller pixel size (Fig. 6(f)). For the long exposure no iterative refinement was necessary due to the better signal-to-noise ratio. The short exposure data set shows an isotropic resolution up to 70 nm half period length. In horizontal direction structures up to 50 nm resolution are visible. For the long exposure data set the Siemens star signal is isotropically resolved up to 40 nm. In the vertical direction the PSD shows spatial frequencies beyond 30 nm resolution.

Fig. 7(d) shows the average value with the standard error illustrated as background area. This procedure is performed for the Holo-TIE reconstructions in the KB- and WG-setup as well as for all images in Fig. 7. The resulting difference values between the bright and dark areas are shown in the table in Fig. 7(d). The theoretical phase shift difference for 500 nm Tantal can be calculated with values from [23] to $\Delta\phi = 0.497$rad for $E = 13.8$ keV and to $\Delta\phi = 0.503$ rad for $E = 13.6$ keV. As can be seen only the value in Fig. 6(f) matches within the expected errors. It is noteworthy that this reconstruction was carried out with the smallest regularization parameter. As this parameter increases to correct higher spatial frequencies, the reconstructed phase shift differences get smaller. This effect can be partially compensated by the use of the hybrid approach, which slightly decreases the gap between the theoretical and measured difference. Note that the theoretical values [23] assume ideal crystalline density, which cannot be expected for the thin film Ta growth process. Previous investigations of the test structure by ptychography had also yielded somewhat lower phase shifts for the test object [38].

The dose of the images was estimated as in [39]

$$D = \frac{\mu I_0 h\nu}{\rho} \,, \tag{11}$$

with $h\nu = 13.6$ keV the photon energy, $\mu$ the linear attenuation coefficient, $\rho$ the density and $I_0$ the fluence. The values for $\mu$ and $\rho$ are taken from [23] and the incident number of photons was measured with a photon counting detector (Pilatus, Dectris). For example, in the 'WG-setup' setting, the dose of the short ($t = 5$ s) and long ($t = 100$ s) exposure data sets is calculated to $D = 4.4 \cdot 10^4$ Gy and $D = 8.8 \cdot 10^5$ Gy, respectively. In order to further quantify the performance, it is important to determine the image resolution. To this end, simple line scans can be analyzed, assuming a perfectly aligned and fabricated edge. For example, a line scan in Fig. 7(c) yields a full width at half maximum (FWHM) of 59 nm. However this resolution may change at other positions and different directions in this image. To get better estimators for the resolution

#179352 - $15.00 USD Received 21 Nov 2012; revised 16 Dec 2012; accepted 16 Dec 2012; published 23 Jan 2013

of the reconstructions, the power spectral density (PSD) has been computed. To improve the visibility of structures in the PSD, a so called Kaiser window was applied prior to the Fourier transform [40].

Figure 8 shows the PSDs for two reconstructions: In (a) the PSD of the hybrid approach with Holo-TIE initial guess (Fig. 7(c)) is shown. The three rings denote different spatial frequencies corresponding to 70 nm (solid line), 60 nm (dashed line) and 50 nm (dotted line) half period resolution. The PSD shows typical spatial frequencies of the Siemens-star which reach 70 nm in all directions. The horizontal lines reach much higher spatial frequencies beyond 50 nm consistent with the visibility of the smallest lines in Fig. 7(c). This anisotropy in the PSD could be explained by the astigmatism of the waveguide, which may not have been fully corrected by the reconstruction. Figure 8(b) shows the PSD for the Holo-TIE reconstruction of the long exposure time data set (Fig. 6(f)) in which no iterative refinement was done. The PSD of this reconstruction shows significantly improved resolution. All directions show structures up to a spatial frequency corresponding to 50 nm resolution which is in good agreement with the visibility of the lines in the inset of Fig. 6(f). In most directions contributions of the Siemens star up to 40 nm are visible and the vertical streaks in the PSD even reach values beyond 30 nm. Note that in order to test for better resolution, other patterns have to be used, since the pattern height of 500 nm easily leads to a broadening on the order of 20 nm, if angular misalignment or fabrication errors are present.

Propagation based phase contrast is a dose efficient imaging technique, in particular in the highly coherent waveguide setting. Compared to diffractive far-field imaging which often necessitates minimum threshold intensities in order for the reconstruction algorithms to work, images can be reconstructed at a wider range of doses. While future work will be directed to a more systematic assessment of the dose-resolution relationship in propagation imaging, the present results also indicate that the technique is very competitive in particular for x-ray imaging applications of large field of view / medium resolution and low dose. Experimental settings, image parameters and the Holo-TIE reconstruction approach make up an almost ideal match, awaiting future applications in imaging and tomography.

**Acknowledgment**

We thank Christian Olendrowitz, Markus Osterhoff, Sebastian Kalbfleisch as well as Michael Sprung and the P10 team for related collaborations in operating the P10 GINIX instrument. Funding by the DFG collaborative research center SFB 755 ‘Nanoscale Photonic Imaging’ and the German Ministry of Education and Research (BMBF-Verbundforschung, Grant No. 05K10MGA) is gratefully acknowledged.

#179352 - $15.00 USD Received 21 Nov 2012; revised 16 Dec 2012; accepted 16 Dec 2012; published 23 Jan 2013